Ion core switching during photodissociation dynamics via the Rydberg states of XeAr

Cailum M.K. Stienstra [a], Alexander Haack [a,b], Arthur E. Lee [a], W. Scott Hopkins [a,*]

[a] Department of Chemistry, University of Waterloo, Waterloo, Ontario N2L 3G1, Canada
[b] Department of Sensors and Measurement Technology, Institute of Electrical Engineering and Measurement Technology, Leibniz University Hannover, 30167 Hannover, Germany

ARTICLE INFO

ABSTRACT

The heterodimer, XeAr, is a classic example of a weakly bound van der Waals molecule, which has a variety of accessible bound excited states that exhibit complex interactions. In this study, XeAr has been investigated in the 77,500–81,500 cm^{-1} region using a combination of Resonance Enhanced Multi-Photon Ionization (REMPI) spectroscopy and Velocity Map Imaging (VMI). By monitoring REMPI and photodissociative product channels across the spectrum, several novel excited states, product channels, excited state symmetries and lifetimes, as well as highly localized perturbations were observed and characterized, including the first VMI study of Ar* dissociating from XeAr Rydberg states accessed by two-photon excitation. In this work we have analyzed 38 vibronic bands representing nine different electronic transitions, and we provide new assignments for two $0^+ \leftarrow 0^+$ electronic transitions dissociating to the Xe* $5d$ $[3/2]_2^0$ (ca. 80,323 cm^{-1}) and Xe* $5d$ $[7/2]_3^0$ (ca. 80,970 cm^{-1}) limits. Several new predissociation product channels were identified at the two- and three-photon levels, including production of Xe* $5p[5/2]_3$, Xe* $6s'[1/2]_1^0$, Xe* $6p[1/2]_1$, Ar* $4p[1/2]_0$, Ar* $4p'[3/2]_1$, Ar* $4p'[1/2]_1$, and Ar* $4p[5/2]_3$. Using the multidimensional analysis offered by VMI, we explore interesting photophysics whereby a resonant state that is reached after absorbing two photons can predissociate to yield Xe*, but which also can absorb a 3rd photon, yielding super-excited Ar*Xe that predissociates to Ar* limits. The ground state dissociation energy for XeAr was determined to be $D_0 = 114.4 \pm 2.7$ cm^{-1}, in excellent agreement with previous measurements.

1. Introduction

Discovered in 1898 through the fractional distillation of its elemental group homologue, krypton, xenon has a history that is fitting for its etymological origin, deriving from the Greek word *xenos*, meaning strange or foreign one.[1] For its first 30 years in the scientific corpus, xenon was viewed as being largely unreactive until Pauling calculated its ionization potential (12.1 eV) and determined that compounds such as XeF_6 and XeO_6^{4-} should be chemically stable.[2,3] Although Pauling was unable to synthesize these compounds, xenon's chemical bonding breakthrough came in 1962 when Bartlett *et al.* mixed PtF_6 with Xe to produce a yellow solid they determined to be $Xe^+PtF_6^-$.[4] From this point, xenon chemistry flourished in a cascade of discoveries in the form of other xenon fluorides, oxides, and a variety of halides.[3,4] Xenon has even been shown to form stable species with unreactive and exotic elements in the creation of $AuXe_4^{2+}$.[5]

Xenon and its derivatives have found practical uses since these inaugural discoveries. Traditional applications include its use as a laser gain medium,[6] in incandescent lamps,[7] in semiconductor silicon etching,[8] and even in modern medicine.[9] Xenon's high polarizability (20× that of helium), endows it a preference for hydrophobic cavities in protein crystallography[1] as well as even in anaesthetics.[9] J. H. Lawrence discovered that xenon had narcotic properties in mice in the 1940s [10] and it has since grown to be viewed as an ideal sedative inhalation agent, with 325,000 L now being used in hospitals annually. [9] Further still, radioactive xenon (^{133}Xe) is used in nuclear medicine as the cornerstone of pulmonary perfusion single-photon emission computerized tomographic (SPECT) imaging.[11] Xenon is also employed at the forefront of modern particle physics; liquid xenon detectors were first imagined by Luis Alvarez at Berkeley to construct a proportional counter for monitoring cosmic radiation.[12,13] Xenon's unique physicochemical properties improved the spatial resolution by

* Corresponding author.
E-mail address: shopkins@uwaterloo.ca (W.S. Hopkins).

several orders of magnitude, achieving a resolution of 10 μm in 1971. [12] As of 2021, liquid xenon detectors are still used because of the element's density and high polarizability, most notably in the XENON project, which aims to identify dark matter in the universe.[13].
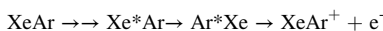
Rare gas dimers are archetypes in the study of rare gas complexes. Xenon's dense electron cloud and polarizability allows it to form stable physically-bound complexes. In 2016, atomic force microscopy of xenon and other rare gases was used to directly measure the magnitude of the van der Waals interaction scales of Xe_2, XeKr and XeAr.[14] While XeAr has been more practically studied as a laser gain medium,[6,15,16] its key purpose in research to date is as an avenue to assess fundamental physicochemical properties of xenon and argon (see, for example, reference [17]). Experimental methods investigating the structure and properties of XeAr, include Resonance Enhanced Multi-Photon Ionization (REMPI),[18–24] fluorescence studies,[16,25] Pulsed Field Ionization Zero Kinetic Energy (PFI-ZEKE)[26-30] photoionization spectroscopy,[31–33] and molecular/photo- emission spectroscopy. [34–36] Several theoretical studies have also explored the structure and properties of XeAr [37–39].

As discussed in our previous work on Kr_2, there are several processes by which photofragments are formed in velocity map imaging (VMI) experiments of rare gas dimer systems.[40] It is important to note that since the ionization threshold of argon ($IE_{Ar} = 127,056$ cm^{-1}) is much higher than that of xenon ($IE_{Xe} = 97,833$ cm^{-1})[41], three-photon excitations are possible for the XeAr heterodimer (and necessary to access Ar* states). Hence, one should consider both sets of photoproducts in the analysis of photofragmentation dynamics experiments. Important process to consider are:
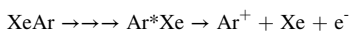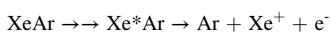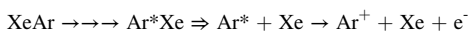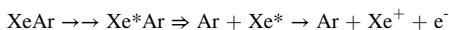
1. (2 + 1) REMPI:

XeAr →→ Xe*Ar → XeAr$^+$ + e$^-$

2. (2 + 1 + 1) REMPI

XeAr →→ Xe*Ar→ Ar*Xe → XeAr$^+$ + e$^-$

3. Dissociative photoionization (DP)

XeAr →→ Xe*Ar → Ar + Xe$^+$ + e$^-$

XeAr →→→ Ar*Xe → Ar$^+$ + Xe + e$^-$
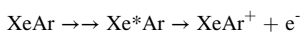
4. Predissociation followed by fragment ionization

XeAr →→ Xe*Ar ⇒ Ar + Xe* → Ar + Xe$^+$ + e$^-$

XeAr →→→ Ar*Xe ⇒ Ar* + Xe → Ar$^+$ + Xe + e$^-$

Here → denotes photon absorption and ⇒ denotes dissociation.[42] The asterisks indicate the center of photoexcitation. Note that for the dissociative photoionization process, the second arrow indicates absorption followed by prompt dissociative photoionization. In the case of (2 + 1 + 1) REMPI (process II), ion core switching at the three-photon level transfers excitation from the Xe center to the Ar center. An analogous process has also been studied in the Rydberg states of the XeKr system.[43]

Upon dissociation, concentric spheres of photofragments (known as Newton spheres) are produced whose radius is proportional to the kinetic energy release (KER) associated with a given product channel. These product channels manifest in photofragment images as a series of rings from which exact kinetic energies can be calculated.[44] Photofragment angular distributions result from the alignment of the molecular transition dipole moment with the laser electric field vector of the plane-polarized laser.[45] The anisotropies of these distributions depend on the electronic symmetries of the intermediate electronic states and their lifetimes. A more thorough discussion of VMI fundamentals can be found in reference 44. Two-photon excitation recoil

anisotropies have been derived by Sander and Wilson[46] and Zare,[45] which were then generalized by Dixon[47] for all possible recoil anisotropy distributions for two and three-photon dissociation processes. The angular intensity distribution from a photo-fragmentation event can be modelled by:

$$I(\theta) \propto 1 + \sum_{k=1}^{n} \beta_{2k} P_{2k}(cos\theta) \qquad (1)$$

where θ is the angle between the fragment velocity vector and the laser polarization vector, β_{2k} are anisotropy fitting parameters and P_{2k} are the even-order Legendre polynomials with degree 2 k.[48] This expression can be expanded to n terms (summing only over even values) where n is the number of photons involved in the fragmentation process. Without considering any smearing or correlation effects, the bounds for anisotropy parameters following one photon excitation are $\beta_2 \in [-1, 2]$, and $\beta_2 \in \left[-\frac{10}{7}, \frac{20}{7}\right], \beta_4 \in \left[-\frac{12}{7}, \frac{8}{7}\right]$ for two photon excitation processes. [48] For three-photon excitation, those bounds change to $\beta_2 \in \left[-\frac{5}{3}, \frac{10}{3}\right]$, $\beta_4 \in \left[-\frac{21}{11}, \frac{24}{11}\right], \beta_6 \in \left[-\frac{40}{3}, \frac{10}{11}\right]$. [48] A more detailed description of theoretical background of photofragment anisotropy is available in Refs. [48,49].

In this study, we explored the XeAr REMPI spectra and the photo-fragment velocity map images for Xe$^+$ and Ar$^+$ (produced via ion-core switching) generated via resonant excitation for 38 vibronic states associated with 9 electronic transitions. For all photofragment images associated with specific product channels, we fit angular distributions to equation (1).

2. Experimental methods

The experimental apparatus has been previously discussed in detail [40] and a schematic diagram can be found in Figure S1. The molecular beam is produced by injecting the precursor gas mixture into a high vacuum chamber using a pulsed solenoid valve. XeAr is formed using 7 % xenon (99.999 % pure) co-expanded in argon (99.999 % pure) from a stagnation pressure of approximately 6 bar into a vacuum chamber at a base pressure of *ca.* 10^{-7} bar. The molecular beam is skimmed 20 cm downstream by a 1 mm diameter molecular beam skimmer (Beam Dynamics, Dallas, USA). The molecular beam then passes into the time-of-flight (ToF) chamber (~10^{-10} bar, length = 70 cm), where it is interrogated with the output of a frequency-doubled tunable, pulsed laser system.

The laser apparatus consists of an optical parametric oscillator (OPO, Continuum Horizon II, 10 Hz, $\Delta\lambda = 0.01$ *nm*) pumped by the 3rd harmonic of a frequency-tripled Nd:YAG laser (Continuum Powerlite). Prior to entering the ToF chamber, the laser light is focused using a spherical lens (Thorlabs, f = 15 mm) onto the center of the molecular beam. The electric field vector of the laser is oriented parallel to the chevron MCP/ phosphor screen detector and perpendicular to the molecular beam. A power meter (Gentec QE25LP/Maestro) located on the opposite side of the ToF chamber was used to measure the excitant light. Laser power varied from 1.8 to 2.3 mJ per pulse across the spectral region that was studied.

With adjustable repeller (V_R) and extractor (V_E) voltages, the instrument supports ToF and VMI modes of operation. In ToF mode (V_R/ $V_E = 1.06$), we record all mass channels simultaneously and separate species based on their flight times through the field-free drift region. Optimal ToF resolution corresponds to a mass-to-charge (*m/z*) resolution of *ca.* 1 amu, but this resolution is reduced when operating in VMI mode. Consequently, when operating in VMI mode, we are unable to resolve the different isotopes of Xe and isotopologues of XeAr, but molecular species and atomic photofragments (*i.e.*, Xe$^+$ and Ar$^+$) are easily resolved.

In VMI mode ($V_R/V_E = 1.52$), the photodissociation of XeAr and subsequent ionization of the neutral atomic photoproducts results in the

formation of concentric spheres of Xe^+ and Ar^+. As the photofragments transit the ToF chamber, the spheres expand until they are crushed onto the 2D plane of multi-channel plate detector, which is coupled to a phosphor screen (Photonis Advanced Performance Detector, d = 40 mm). The KER of the photodissociation process and the photofragment drift time define the radius of the observed 2D images. Pulsing the front plate of the MCP from 0 V to 600 V with an appropriately timed delay enables mass-selection of the desired photoproduct. Experimental timings were synchronized using a BNC 575 delay generator.

Photofragment images were captured using a 1280 × 960 CCD camera (Manta G-125B) mounted behind the phosphor screen. Depending on the intensity of the transition, 1000 – 8000 images were obtained for each transition on multiple different days to ensure reproducibility. Images were summed using a Python script and were subsequently processed using the Polar Onion Peeling (POP) code of Roberts et al.[49] We further analyzed photofragment images using a customized version of the PyAbel package[50] (radial integration, anisotropy analysis, Total Kinetic Energy Release (TKER) calculation, *etc.*). A low-pass Fourier filter was implemented to reduce high-frequency noise. Tests showed that Fourier filtering had no effect on the extracted anisotropy terms (cf. Eq. (1)).

3. Results and discussion

3.1. XeAr electronic structure

Heavy rare gas diatomic molecules are categorized by Hund's case C coupling, whereby the interaction between the orbital angular momentum (L) and spin angular momentum (S) is stronger than their coupling with the internuclear axis. As a result, Σ and Λ are not well-defined, but Ω, the projection of the total angular momentum (J) onto the internuclear axis is relevant. Two-photon transitions in XeAr arise from photo-excitation of the X 0^+ electronic ground state and are governed by electronic dipole selection rules: $|\Delta\Omega| \leq 1$, $|\Delta J| \leq 2$, and $+$

$\leftrightarrow +$. [51] Thus, only the 0^+, 1, and 2 excited electronic states are accessible from the ground state for two-photon transitions of XeAr. The potential energy curves (PECs) of XeAr pertinent to this study (derived from all available literature data [20,23–25,33]) are depicted in Fig. 1A. In this figure, we present excited states of Xe*Ar that dissociate to known Xe* ($6s$, $6p$, $5d$) Rydberg state limits (*ca.* 77,000 – 82,000 cm^{-1}), low-lying excited ionic states (*e.g.*, $XeAr^{+*}$ A_1 $^2\Pi_{3/2}$) that dissociate to Xe^+ limits (*ca.* 96,000 cm^{-1} – 110,000 cm^{-1}), as well as Ar* ($4p$) states (*ca.* 105,000 – 110,000 cm^{-1}) that lie above the xenon ionization threshold.

To garner qualitative insights into the electronic structure and nature of the excited states of XeAr, we conducted Hartree-Fock (HF) calculations applying the relativistic Douglas-Kroll Hamiltonian (DKH)[52] for the ground (singlet) states of isolated Xe and Ar as well as the bound XeAr at a bond distance of 4.09 Å, which is the ground state equilibrium bond length.[39] We applied the Sapporo-QZP-2012 basis[53] set for Ar and, to account for relativistic effects of the heavy Xe nucleus, the Sapporo-DKH3-QZP-2012 basis set.[54] In this way, we obtained occupied and virtual orbitals for the three systems (Ar, Xe, XeAr). By performing Löwdin population analysis[55] on the XeAr wavefunction, we were able to determine the contributions of the atomic orbitals (AOs) to the obtained molecular orbitals (MOs), yielding the MO diagram shown in Fig. 1B. Calculations were performed with the ORCA 5.0.4 program suite.[56,57] These MO calculations provide a qualitative picture of the excited states; more accurate calculations of excitation energies or transition probabilities would require more sophisticated methods like those used in reference 40.

As is evident by the MO diagram (Fig. 1B), the six highest occupied molecular orbitals (HOMOs), *i.e.*, four π-type and two σ-type orbitals, consist of the almost unchanged $3p$ and $5p$ AOs of Ar and Xe, respectively. The lack of orbital interaction can be explained by the large energy gap between them. The lowest unoccupied molecular orbital (LUMO) is of σ symmetry and consists of the $6s$ AO of Xe, again not showing significant mixing with other orbitals. At higher energy,
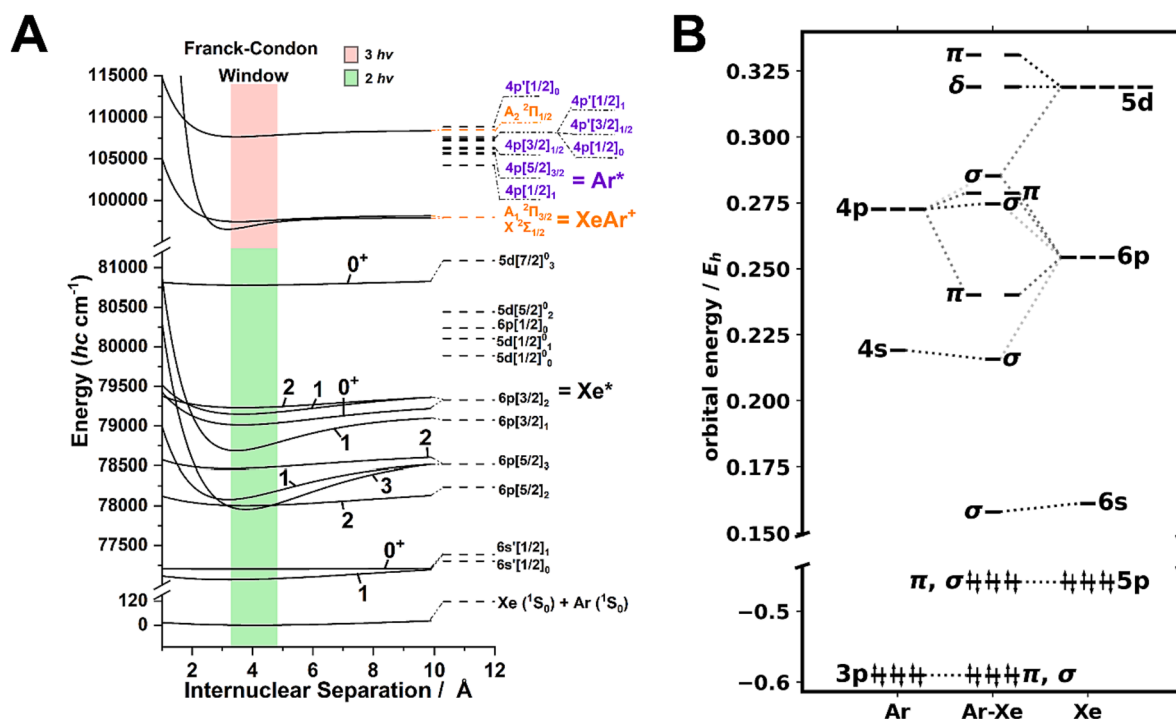

Fig. 1. (A) Potential Energy Curves (PECs) for XeAr in the Xe* $5d/6p/6s$ region alongside the low-lying $XeAr^+$ excited states and XeAr in the Ar* $4p$ region. PECs are derived from Morse potential parameters reported in the literature, with bond lengths slightly adjusted to yield Franck-Condon envelopes consistent with observed spectral stimulus profiles [20,23–25,34]. (B) MO diagram of XeAr derived from a Hartree-Fock calculation using the relativistic Douglas-Kroll Hamiltonian (HF-DKH) and the Sapporo-QZP-2012 basis set for Ar, the Sapporo-DKH3-QZP-2012 basis set for Xe, and an interatomic distance of r = 4.09 Å.

however, the *4s* and *4p* Aos of Ar mix with the *6p* Aos of Xe to form MOs of σ and π type. Small contributions from the *5d* orbitals of Xe are also observed in calculations.

The atomic excited states depicted in Fig. 1A (*i.e.*, separated atom limits on the righthand side) can be understood as excitations from states corresponding to the highest occupied atomic orbitals of the isolated atoms to their respective lowest unoccupied atomic orbital *e.g.*, an excitation from *3p* into *4p* for Ar or from *5p* into *6s* of Xe. For example, two-photon excitation of XeAr promotes electrons occupying the HOMO (corresponding to the Xe *5p* AO valence electrons) to the virtual MOs where the excitation is localized on the xenon atom, which we denote Xe*Ar. If dissociation occurs at this point, a Xe* Rydberg state and Ar [1] S_0 are produced. Alternatively, the Xe*Ar molecule can absorb a third photon, resulting in photo-ionization to yield $XeAr^+$ via a (2 + 1) REMPI process. A schematic illustration of this effect can be observed in figure S2. In our experiments, we also observe Ar^+ photoproducts (see below). Ion core switching to create a super-excited neutral state (*i.e.*, a neutral state existing above the ionization threshold) is a possible explanation for this behaviour.[42] At the three-photon level, there exist neutral states associated with excitation of the Ar atom above the lowest lying ionization thresholds. Accessing these via the bound Xe*Ar states at the two-photon level effectively occurs via promotion of an electron from one of the localized *3p* Ar MOs to an MO corresponding to the Xe *5p* AOs. We refer to these super-excited states in the text as Ar*Xe, where the excitation is localized on the argon moiety. Upon dissociation of Ar*Xe, the Rydberg electron converges to the argon *4p* orbitals and instead Ar* + Xe $^1S_0$ is produced. This phenomenon has been previously documented in the photofragment spectrum of ArKr,[42] as well as in cases of bimolecular collisions between rare gas molecules[58] and other species.[59,60] At the time of writing this manuscript, Fukuda et al. reported a study of the analogous KrXe system, where ion-core switching to yield Kr^+ was observed.[43].

Since the Xe *5p* AOs (corresponding to the HOMO) lie higher in energy than the Ar *3p* AOs, it takes less energy to excite the Xe electrons into the molecular LUMOs than it does the Ar electrons. For example, excitations from the MOs corresponding to the Xe *5p* AOs into the lowest π MOs occur in the 77 000 – 82,000 cm^{-1} region, whereas excitations from the MOs corresponding to the Ar *3p* AOs (to the same excited π Mos) occur in the 105,000 – 115,000 cm^{-1} region (see Fig. 1A). These Ar*Xe states lie above the first ionization threshold of XeAr (IE$_{XeAr}$ = 96,545 cm^{-1}). [26,28,30].

To further model the ion core switching mechanism using *ab initio* methods, more advanced methods like those employed in reference 40 would be needed to explicitly determine the excited state (*e.g.*, Xe*Ar, Ar*Xe) PECs. The dipole overlap of electronic/vibrational wavefunctions can then be used to calculate likely transition probabilities. However, owing to the limitations of the Born-Oppenheimer approximation (*e.g.*, in treating avoided crossings), these calculations cannot approach experimental precision and, ultimately, measurement is still required to garner an accurate picture of these excited state interactions.

3.2. REMPI and UVPD spectra

Fig. 2 shows the experimental REMPI spectrum of XeAr in the 77,500 – 81,500 cm^{-1} region, along with the UltraViolet PhotoDissociation (UVPD) spectrum obtained by monitoring the Xe^+ and Ar^+ product channels. Wavenumber values at the two-photon level and have been calibrated to align with atomic transitions reported by NIST.[61] We expect that the REMPI spectrum shown in Fig. 2 is associated with a (2 + 1) resonant photo-ionization process because the observed band systems are associated with known XeAr transitions at the two-photon level. However, observation of Ar^+ photofragments indicates that (2 + 1 + 1) photoexcitation, whereby resonant states exist at the two- and three-photon levels, is also possible. The vibronic band assignments are
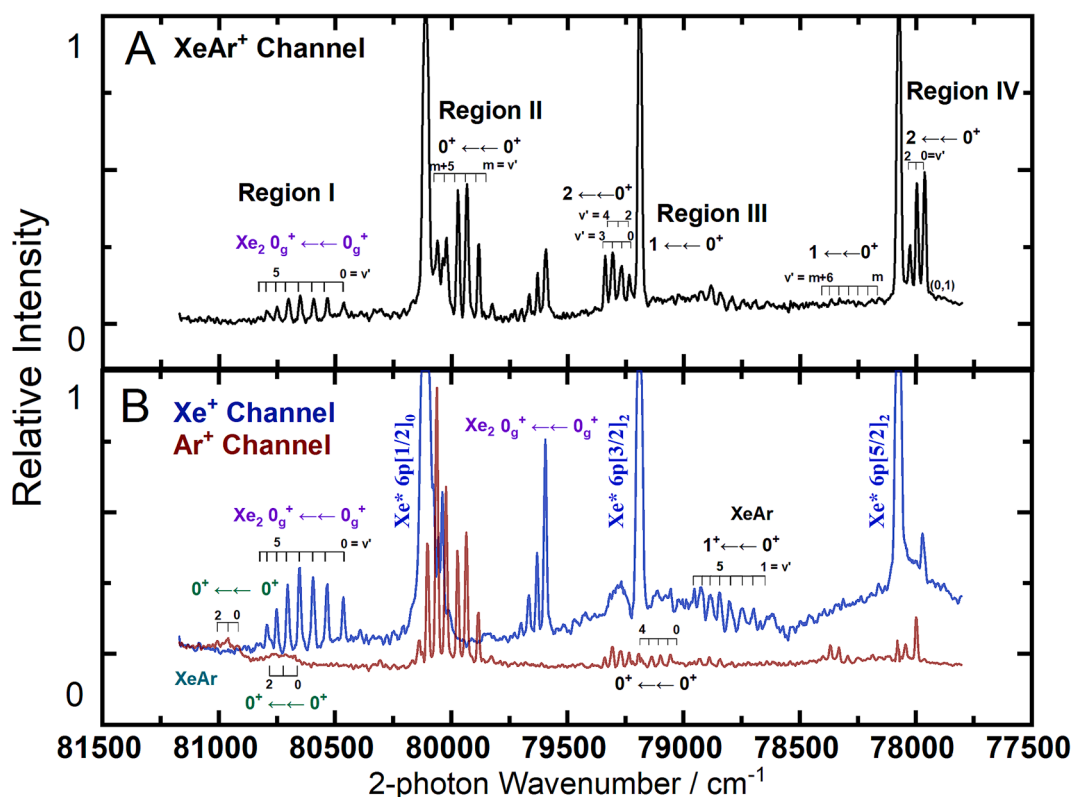

Fig. 2. Overview of the XeAr (N + M) REMPI Spectrum in the vicinity of the 6*p* and 5*d* Xe* atomic limits. Literature assignments are taken from Refs. [22–24,32–33] and atomic line positions are taken from reference 56. Xe* atomic lines are observed in both the Xe^+ and $XeAr^+$ channels due to detector saturation. Xe_2 transitions are labelled in purple font. New XeAr band assignments are shown in teal font. Xe^+ and Ar^+ spectra represent photoproducts generated from ultraviolet photodissociation (UVPD).

made in accordance with those reported in Refs. [21,23,25,32]. Band assignments are discussed in pertinent sub-sections below. Rotational features within a vibrational band were not resolved because the rotational constant of the ground state molecule is several orders of magnitude smaller than the resolution of our laser system.[27] In our analysis, we considered only the $^{131}Xe^{40}Ar^+$, $^{131}Xe^+$, and $^{40}Ar^+$ mass channels; ^{131}Xe is the centre of the Xe isotopic distribution and Ar is 99.5 % naturally abundant as ^{40}Ar. When exciting each of the XeAr vibronic bands observed, Xe^+ and Ar^+ photofragments were produced and analyzed via VMI. We divide the spectrum into four regions (I, II, III, and IV) based on the observed Xe atomic transitions to streamline our discussion (see Fig. 2). A full list of transition frequencies, band assignments, and product channel assignments is available in the supporting information.

3.3. Region I: 81,200 – 80,250 cm^{-1}

At the high-wavenumber end of the spectrum (Region I), we observe a well-resolved band system starting at *ca.* 80,500 cm^{-1}. These transitions, which are associated with the xenon dimer, agree well with the $0_g^+ \leftarrow 0_g^+$ band positions and intensities obtained by Hu et al. in their REMPI study of Xe_2.[62] While our instrument is capable of 1 amu resolution, the very intense Xe^+ signal generated via photodissociation of Xe_2 in this region saturates our detector and leaks over into the $XeAr^+$ mass channel. Hu proposed that the perturbation observed in the vibrational levels is due to an avoided crossing in this region, giving rise to predissociation.[62] Consequently, we also observe this band system in the Xe^+ product channel (see Fig. 2B). When imaging the Xe^+ fragments that are produced via these known Xe_2 vibronic bands, we observe products of predissociation to the Xe* $6p[1/2]_0$ + Xe $^1S_0$ threshold (See Fig. 3). Energy balance calculations yield a ground state dissociation energy of $\sim$ 200 cm^{-1}, which agrees well with the literature value of $D_0''(Xe_2) = 196.1$ cm^{-1}. [63].

XeAr exhibits two-photon electronic transitions in the 78,000 – 81,000 cm^{-1} region, analogous to those of Xe_2, but involving states that correlate with the nearby Xe* + Ar $^1S_0$ separated atom limits. Photofragment imaging across this spectral region shows dissociation to generate high- and low- TKER Xe^+ photoproducts, as well as Ar^+. In Region I, the XeAr transitions are most apparent in the Ar^+ product channel (see Fig. 2B), which exhibits two poorly resolved band systems that were previously reported by Khodorkovskii.[23] Between 80,600 – 80,700 cm^{-1}, they observed a short vibrational progression involving an excited state that they conclude correlates to the Xe* $5d$ $[3/2]_2^0$ + Ar $^1S_0$ separated atom limit, and they reported a longer progression between 80,800 cm^{-1} – 81,000 cm^{-1} for which the excited state correlates to the Xe* $5d$ $[7/2]_3^0$ + Ar $^1S_0$ separated atom limit. The study by Khodorkovskii was unable to offer comment on the symmetries of these excited states, but we offer some insights below. Images of Xe^+ indicate that predissociation of XeAr occurs at the two-photon level to access the Xe* $6p$ $[3/2]_2$ + Ar $^1S_0$ product channel (see Fig. 3). The Xe^+ angular distributions measured across Region I are weakly anisotropic. The transition at *ca.* 80,690 cm^{-1} yields $\beta_2, \beta_4, \beta_6$ = 0.31, –0.05, –0.03, respectively, and a slight increase is observed for the β_2 term with increasing vibrational number (*e.g.*, the transition at *ca.* 80,773 cm^{-1} yields $\beta_2, \beta_4, \beta_6$ = 0.48, –0.06, –0.02, respectively). This trend in image anisotropy suggests that exited states are somewhat shorter-lived at higher energy.

Images of Ar^+ photofragments in this spectral region yield TKERs on the order of 10,000 cm^{-1}. Regression of the TKER for the observed Ar^+ products as a function of three-photon excitation wavenumber indicates that predissociation occurs at the three-photon level. Energy balance calculations indicate that this predissociation accesses the Ar* $4p$ $[1/2]_0$ + Xe $^1S_0$ product channel (see Fig. 4). All product channels discussed in this work with associated labels and photodissociation processes are available in Table S1. The Ar^+ product angular distributions are strongly anisotropic and may be described by a single anisotropy parameter of $\beta_2 \approx 1.25$; higher-order contributions of β_4 and β_6 are both less than 0.2. These anisotropies indicate fast predissociation following absorption of the third photon, where correlation of center of mass velocity (μ) and tangential velocity (ν) results in effective cancellation of the higher order terms.[42,64].

The observed photoexcitation and photodissociation behaviour suggests that ion core switching is occurring at the three-photon level, as was discussed earlier when referring to the molecular orbital diagram
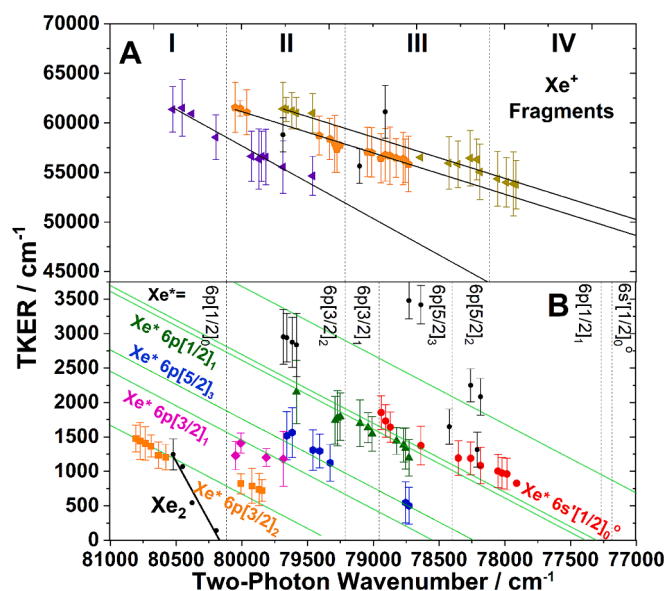

Fig. 3. Xe^+ photofragment TKER regression across the spectrum for (A) high TKER dissociative ionization channels as well as (B) two-photon low TKER-predissociation Xe* limits[61] with theoretically calculated predissociative channels (green lines). TKER errors were determined by fitting TKER peaks to Gaussian curves and are reported as ±1 σ.

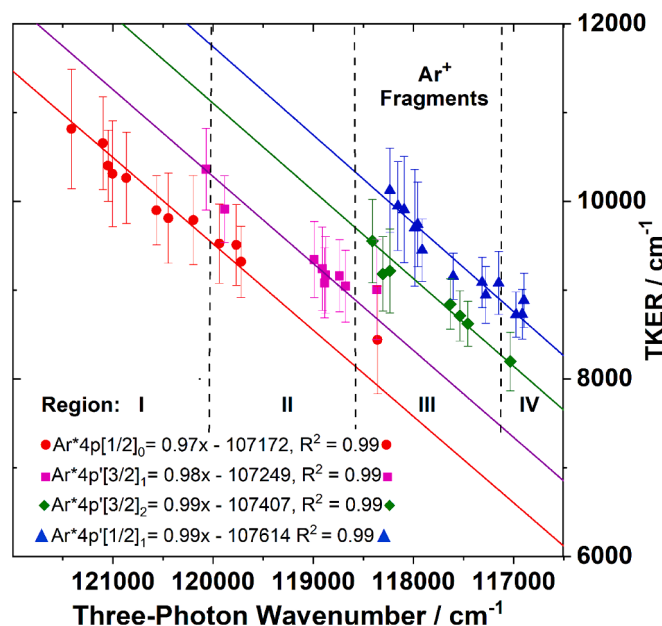**Fig. 4.** TKER Analysis of Ar^+ photofragments across the spectral region at the three-photon level with associated regression assignments. Assignments were made using regression of the raw data. Plotted trendlines and reported fit parameters represent least squares regression completed with an intercept fixed at the assigned literature x-intercept value. TKER errors were determined analogously to Xe^+ photofragments.

shown in Fig. 1B. This phenomenon is notable because, at the two-photon level, the electronic excitation is localized on the xenon moiety (*i.e.,* Xe*Ar, with predissociation yielding neutral Xe*), but upon absorption of a third photon, charge transfer occurs, and the electronic excitation becomes localized on the Ar moiety. This process yields a neutral super-excited Ar*Xe state that exists above the lowest ionization threshold. Thus, we observe an interesting competition arising between several different product channels. At the two-photon level, Xe*Ar either predissociates to produce Xe* or absorbs a third photon, which either ionizes the parent molecule or induces charge transfer to yield Ar*Xe. The super-excited Ar*Xe molecule can either undergo detachment to yield the molecular ion (by coupling to ionic XeAr$^+$ states that correlate with Xe$^+$ states near the ionization threshold), photoionization via $(2 + 1 + 1)$ REMPI, or predissociation to yield Ar* $4p$ $[1/2]_0$, which is subsequently ionized with a 4th photon. In other regions (see below), Ar$^+$ photofragments are observed with $\beta_2 > 2$, which indicates that Ar*Xe formation occurs as a three-photon excitation. As such, it seems that these Ar$^+$ predissociation processes should be thought of as arising from continuous three photon excitation, rather than as two-step process involving a long-lived intermediate state.

Nevertheless, the relatively isotropic Xe$^+$ angular distributions indicate that the resonant state at the two-photon level is relatively long-lived on the molecular rotation timescale. Moreover, the Xe$^+$ angular distributions in this region are slightly more anisotropic than those in other regions (*vide infra*), and we observe slightly lower Ar$^+$ signal in this region compared to those other regions, suggesting that the lifetime of the Xe*Ar states at the two-photon level does impact the probability of accessing super-excited states at the three-photon level.

Based on the theory outlined by Dixon, the only possible three-photon XeAr photodissociation processes that can possess a large, positive value of β_2 for the Ar* photofragment are of the form $0^+ \rightarrow \rightarrow \rightarrow 0^+$ or $0^+ \rightarrow \rightarrow \rightarrow 1$. Given the relatively large, positive values of the β_2 parameter for the Ar$^+$ images, and the fact that the excited molecular state corresponding to the Ar* $4p$ $[1/2]_0$ limit only can have a symmetry of 0^+, we expect that the electronic transition occurs via $0^+ \rightarrow \rightarrow \rightarrow 0^+$ excitation. [47] Since the excited electronic states observed by Khodorvskii at the two-photon level (correlating to the Xe* $5d$ $[3/2]_2^0$ and $5d$ $[7/2]_3^0$ limits) access the Ar* $4p$ $[1/2]_0$ 0^+ state at the three photon level, and because the observed Ar$^+$ angular distributions indicate prompt dissociation via parallel excitation to a 0^+ state, we favour 0^+ symmetries for both of the states at the two-photon level.

It is noteworthy that the Xe$^+$ photofragments across this spectral region also exhibit a series of high-TKER ($\sim$60,000 cm^{-1}) product channels observed at the limit of our MCP detector (see Fig. 3). Regression of the high-TKER product channel at the two-photon level yielded an asymptotic limit below any accessible neutral Xe* states, and at the three-photon level produced no clear asymptotic limit to known atomic states. Similar high-TKER Xe$^+$ products are observed in other spectral regions (see Fig. 3A). Interestingly, the angular anisotropy distributions of these high TKER photofragments are well described by a single-photon process involving prompt dissociation following a parallel transition.

To deduce the origin of the high-TKER Xe$^+$ photofragments, we must consider the low-lying dissociative thresholds of the molecular cation. In 1985, Pratt *et al.* first studied XeAr$^+$ using REMPI photoelectron spectroscopy (REMPI-PES) and reported on the X $^2\Sigma_{1/2}$, A_1 $^2\Pi_{3/2}$, A_2 $^2\Pi_{1/2}$ states, which correlate with the Xe$^+$ $^2P_{3/2}$ + Ar $^1S_0$ and the Xe$^+$ $^2P_{1/2}$ + Ar $^1S_0$ thresholds.[32] A more recent experimental work on XeAr$^+$ was completed by Piticco *et al.* who used rotationally resolved pulsed-field-ionization zero-kinetic-energy photoelectron spectroscopy (PFI-ZEKE) to perform high-resolution rovibronic studies on the low-lying states between 90,000 – 120,000 cm^{-1}.[26,28–30].In these studies, XeAr$^+$ was produced via $(1 + 1')$ REMPI of the neutral XeAr molecule. The molecular constants determined in these works were employed to calculate the potential energy curves shown in Fig. 1. Given that the XeAr$^+$

dissociation thresholds that produce Xe$^+$ occur at *ca.* 100,000 cm^{-1} above the neutral ground state,[27,32] and that we observe photo-excitation processes up to the 4-photon level, it is likely that the high-TKER Xe$^+$ products are formed via dissociative photoionization at $4h\nu \approx 160,000$ cm^{-1} to yield Xe$^+$ $^2P_{1/2}$ or Xe$^+$ $^2P_{3/2}$ with TKER $\approx 60,000$ cm^{-1}. However, because we are unable to detect the correlated photo-electron, which will also carry some amount of kinetic energy and exhibit some degree of angular anisotropy, we cannot report a definitive assignment. Similar observations and interpretation were reported for Xe$_2$.[63] The TKERs of the high energy Xe photoproducts are provided in the SI. Given the ambiguities in product assignments, we have chosen not to provide definitive assignments here.

3.4. Region II: 80,300 – 79,200 cm^{-1}

Transitions between 80,300 cm^{-1} – 79,500 cm^{-1}. Fig. 5 shows the REMPI and UVPD spectra observed in the vicinity of the Xe* $6p$ $[1/2]_0$ – $^1S_0$ atomic transition at 80,109 cm^{-1}. This band system is associated with the $0^+ \rightarrow \rightarrow 0^+$ transition correlating to the Xe* $6p$ $[1/2]_0$ + Ar $^1S_0$ separated atom limit.[20,24] Xe$^+$ photofragment images indicate that predissociation occurs to access two product channels (see Fig. 3). The first product channel is associated with predissociation to Xe* $6p$ $[3/2]_2$ + Ar $^1S_0$ as was observed in the spectral region to higher energy. We also observe photofragments to higher TKER that we tentatively assign to the Xe* $6p$ $[3/2]_1$ predissociation channel (Fig. 3, pink). All low TKER Xe$^+$ photoproducts exhibit relatively isotropic angular distributions ($\beta_2, \beta_4, \beta_6 < 0.3$).

Relatively intense Ar$^+$ signal is observed when exciting via the $0^+ \rightarrow \rightarrow 0^+$ transition in this region. Analysis of the associated Ar$^+$ images indicates that dissociation accesses the Ar* $4p$ $[1/2]_0$ + Xe $^1S_0$ and Ar* $4p'$ $[3/2]_1$ + Xe $^1S_0$ thresholds at the three-photon level (see Fig. 4). Thus, as was discussed above for the Ar$^+$ signal observed via photo-excitation in Region I, the $0^+ \rightarrow \rightarrow 0^+$ band system at *ca.* 80,000 cm^{-1} is acting as an intermediate state via which a third photon can be absorbed to access a super-excited Ar*Xe state that subsequently predissociates.
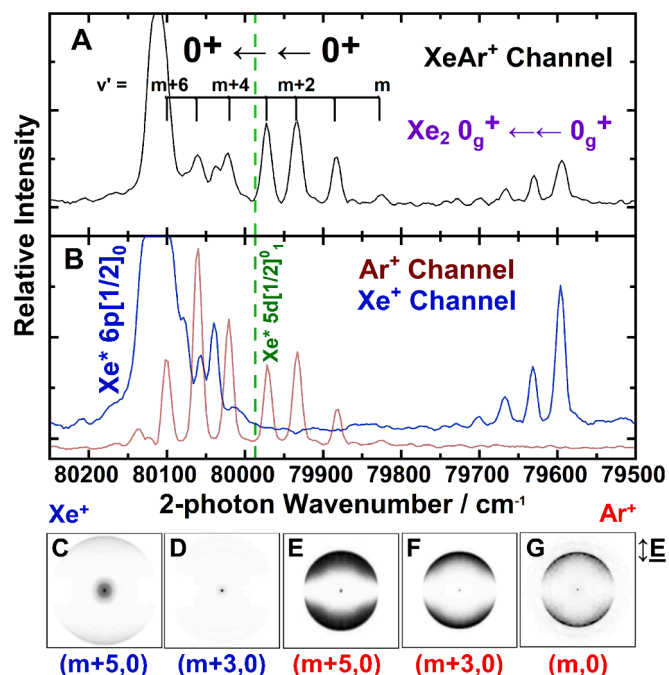

Fig. 5. (**A**) XeAr REMPI spectrum and (**B**) UVPD spectrum in the vicinity of the Xe* $6p$ $[1/2]_0$ atomic transition (Region II; Fig. 2). Select photofragment images (**C-G**) (Xe$^+$: blue, Ar$^+$: red) are displayed alongside the transition via which they were acquired.

The angular distributions observed for the Xe^+ images recorded via the $0^+ \to \to 0^+$ band system are significantly more isotropic in Region II ($\beta_2^{Xe} \approx 0.0$) than they are in Region I ($\beta_2^{Xe} \approx 0.3$). Considered together with the fact that the Ar^+ signal is comparatively more intense in Region II, it seems likely that the lifetime of the 0^+ state in Region II is significantly longer than those of the two 0^+ states accessed in Region I. This interpretation is further supported by the fact that the lower energy vibronic bands for the $0^+ \to \to 0^+$ electronic transition at *ca.* 80,000 cm^{-1} (*i.e.*, the v' = m to v' = m + 3 bands; see Fig. 5) are observed only in the $XeAr^+$ and Ar^+ channels; absorption of a third photon outcompetes predissociation at the two-photon level. In their *ab initio* study, Hickman *et al.* reported evidence of "strong nonadiabatic interaction" between the 0^+ state correlating with Xe* 6p [1/2]$_0$ products and the 0^+ state correlating with Xe* 5d [1/2]$_1^0$ products at 3.7 Å.[39] Given our experimental observations, it seems likely that this interaction becomes significant near the (m + 3, 0) band, at energies above which Xe* predissociation products are observed.

Angular distributions of Ar^+ in this region are similarly anisotropic to those observed at higher wavenumber. In general, we measure large, positive values of β_2 and small, negative contributions from higher order terms (*e.g.*, at 79,813 cm^{-1}, v' = m, $\beta_2, \beta_4, \beta_6$ = 1.74, −0.37, −0.24). These values most closely align with the limiting values of $\frac{5}{3}$, $-\frac{48}{33}$, and $-\frac{40}{33}$ reported by Dixon for a $0^+ \to 0^+ \to 0^+ \to 1$ photoexcitation process. This is in good agreement with Dimov et al.[20] and Khorodosvskii et al. [24], who report assignments of $0^+ \to \to 0^+$ for the two-photon transition.

Transitions between 79,500 cm^{-1} – 79,200 cm^{-1}. Two overlapping electronic band systems are observed in the 79,500 cm^{-1} – 79,200 cm^{-1} region (see Fig. 6). These band systems have previously been assigned to the $0^+ \to \to 1$ and $0^+ \to \to 2$ electronic transitions correlating to the Xe* 6p [3/2]$_2$ + Ar $^1S_0$ separated atom limit.[24] Xe^+ images acquired via the bands at the high-wavenumber end of the system show predissociation to form Xe* 6p [5/2]$_3$ + Ar $^1S_0$ (Fig. 3), but this channel abruptly closes at *ca.* 79,400 cm^{-1} [*i.e.*, the (4, 0) band] and predissociation occurs exclusively to yield isotropically-distributed Xe* 6p [1/2]$_1$ + Ar $^1S_0$ products at lower energies (see Fig. 4). This abrupt change in product branching ratios indicates the presence of a local perturbation in the vibronic structure of XeAr. Precedent for such a perturbation is provided by Hickman *et al.*, whose calculations indicate an avoided crossing between the $\Omega' = 2$ Xe* 6p [3/2]$_2$ and the $\Omega' = 2$ Xe* 6s' [1/2]$_1^0$ potential energy curves at 3.2 Å.[39]

Images of the Ar^+ photofragments produced via the $0^+ \to \to 1$ and $0^+ \to \to 2$ electronic transitions in this region all show formation of Ar* 4p' [3/2]$_1$ + Xe $^1S_0$. Angular distributions are all strongly anisotropic, with large, positive β_2 parameters and minor, negative contributions

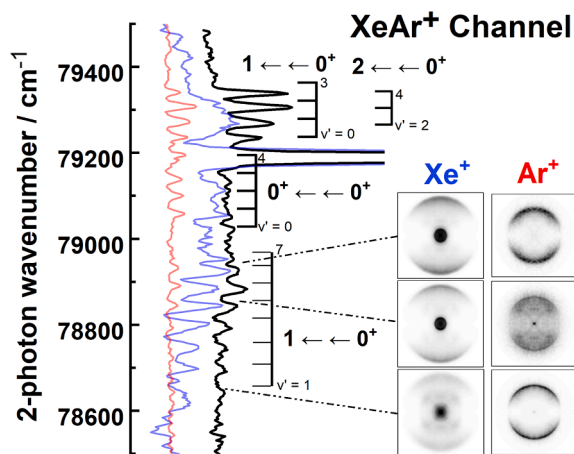from the higher order terms (*e.g.*, at 79,273 cm^{-1}, $\beta_2, \beta_4, \beta_6$ = 1.43, −0.32, −0.12). All Xe^+ photofragments imaged via these band systems are isotropic. It is possible that because the two-photon Xe*Ar intermediate is long lived, a third photon can excite the molecule and induce ion-core switching to yield Ar*Xe, which dissociates to produce Ar*. Based on the work of Dixon, and given the observed Ar^+ anisotropies, it is likely that the three-photon process giving rise to Ar* is $0^+ \to 0^+ \to 1 \to 1$ or $0^+ \to 1 \to 1 \to 1$. [18,64].

3.5. Region III: 79,200 – 78,600 cm^{-1}

3.5.1. Transitions between 79,200 cm^{-1} – 79,000 cm^{-1}

To lower wavenumber of the Xe* 6p [3/2]$_2$ atomic transition there exist two XeAr transitions observed by Khodorokovskii.[24] The first, at approximately 79,100 cm^{-1}, was assigned as the $0^+ \to \to 0^+$ transition correlating to Xe* 6p [3/2]$_1$ + Ar $^1S_0$ limit.[24] Following excitation of this band system, Xe* 6p [1/2]$_1$ photoproducts are observed with essentially isotropic angular distributions.

Images of Ar* photofragments generated via this band system reveal highly anisotropic product angular distributions (*e.g.*, Ar^+ via v' = 2, β_2, β_4, β_6 = 2.31, 0.39, −0.12). Energy balance calculations indicate that predissociation occurs to the Ar* 4p' [3/2]$_1$ + Xe $^1S_0$ threshold. Comparing with the limiting cases reported by Dixon, we favour a $0^+ \to 0^+ \to 0^+ \to 1$ photoexcitation scheme.

3.5.2. Transitions between 79,000 cm^{-1} – 78,600 cm^{-1}

The lowest energy transition in this region, occurring from 79,000 – 78,600 cm^{-1} has been previously assigned as the $0^+ \to \to 1$ transition dissociating to the Xe* 6p [3/2]$_1$ separated atom limit.[24] This transition is allowed by parity but not by the ΔJ selection rule, which is why it is an order of magnitude weaker in intensity than the bands associated with the Xe* 6p [3/2]$_2$ limit.[24] Interestingly, this band is quasi-bound, meaning that some of the vibrational members will be metastable due to a barrier to dissociation. This behavior is also observed in the calculations of Hickman, (curve 2p$_7$ as designated by the paper's internal notation scheme)[39] and exhibits different spectroscopic behavior due to the barrier. This region has the richest variance in dissociation channels observed in the entire study.

For low TKER Xe^+ photofragments, the dissociation channels for this band are markedly different from the neighboring transitions. For v' = 8 and 7 (*ca.* 79,009 cm^{-1}), we see dissociation into the Xe* 6p[1/2]$_1$ channel. These excited vibrational levels are located above the asymptotic limit and enable tunneling through the potential barrier. For transitions to vibronic levels below the Xe* 6p [3/2]$_1$ asymptotic limit (*ca.* 78,956 cm^{-1}), we observe the opening of the Xe* 6s [1/2]$_1^0$ dissociation channel.

The Xe* 6p[1/2]$_1$ dissociation channel stays open until 78,745 cm^{-1} at which point we also see the opening of the Xe* 6p[5/2]$_3$ channel. At this wavenumber, we observe two transitions that are notable because they access three distinct low TKER xenon dissociation pathways. Two of these low TKER product channels are associated with formation of Xe* 6p[1/2]$_1$ and Xe* 6p[3/2]$_1$ (discussed above for dissociation in Region II). The third, which exhibits TKER ~ 3,300 cm^{-1} and anisotropic Xe^+ distributions (β_2 = 0.97, β_4 = -0.67, β_6 = −0.30; see Fig. 7A), must correspond with rapid dissociation following $0^+ \to 0^+ \to 1$ or $0^+ \to 1 \to 1$ excitation processes.[47] Unfortunately, there were too few transitions accessing this dissociation channel to make a confident assignment of the product channel and parent molecule. Based on the magnitude of the TKER values, it is likely that this transition is accessing one of the low lying 6s xenon Rydberg states (*ca.* 68,000 cm^{-1}), however, these observations could also be explained by Xe_2 predissociation to the Xe* 6p [5/2]$_2$ or 6p [5/2]$_3$ states.

Photofragmentation to yield Ar^+ in this region exhibits dissociation to four different channels, with dramatic variation between branching ratios for different excited vibrational states. At v' = 7,8 we observe the
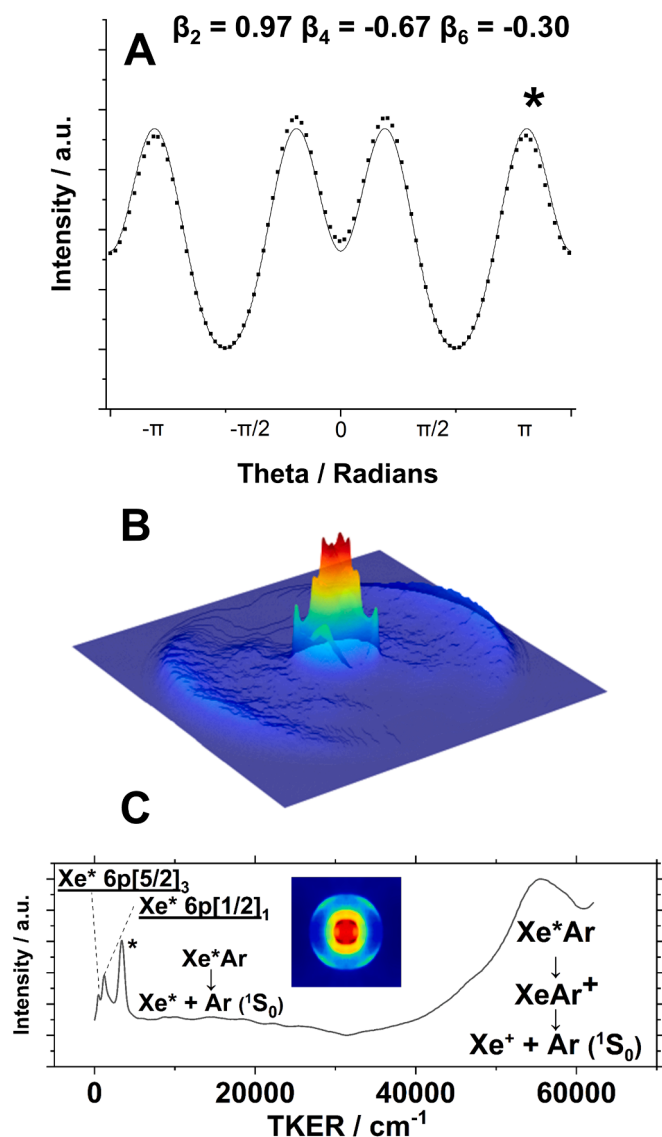

Fig. 6. XeAr$^+$ (2 + 1) REMPI spectrum in the vicinity of Xe* 6p[3/2]$_2$ atomic transition with accompanying Xe$^+$/Ar$^+$ dissociation channels. Select photofragment images are displayed alongside their vibrational level.

Fig. 7. (**A**) Angular product distribution for the unassigned Xe$^+$ product channel (labelled with an astersik), ~3,300 cm^{-1}) accessed via the transition at 78,720 cm^{-1}. (**B**) Photofragment contour plot for the same image, and (**C**) TKER spectrum showcasing the different dissociation pathways.

production of Ar* $4p$'[3/2]$_1$. This channel closes in favor of Ar* $4p$'[3/2]$_2$ production at v'=6. At v' = 5 and v'=4, we observe only the Ar*$4p$'[3/2]$_1$ and Ar*$4p$[1/2]$_0$ product channels, respectively, which then close in favor of the Ar*$4p$'[3/2]$_2$ channel for v' = 3. For v' = 0 – 2, we observe products corresponding to the Ar* $4p$ [1/2]$_1$ dissociation limit. As was the case in other regions, anisotropy analysis of Ar$^+$ photofragments yields large positive β_2 with minor negative contributions from the higher order parameters.

Different dissociation channels yielding Ar* exhibit significant differences in anisotropy parameter, allowing for distinction of dissociation pathways. For example, dissociation via v' = 4 to produce Ar*$4p$[1/2]$_0$ exhibits anisotropy parameters of β_2, β_4, β_6 = 0.99, −0.29, −0.16, whereas dissociation via v' = 0 to Ar*$4p$[1/2]$_1$ exhibits β_2, β_4, β_6 = 1.76, −0.24, −0.21. States exhibiting smaller values of β_2 likely predissociate more slowly than those with larger values. Based on the product assignment and observed anisotropies, we can conclude that this transition occurs via either a $0^+ \rightarrow 0^+ \rightarrow 1 \rightarrow 1$ or $0^+ \rightarrow 1 \rightarrow 1 \rightarrow 1$ pathway.

3.6. Region IV: 78,600 – 77,800 cm^{-1}

3.6.1. Transitions between 78,600 cm^{-1} – 78,100 cm^{-1}

Region IV is characterized by the presence of the Xe* $6p$ [5/2]$_2$ atomic transition at 78,071 cm^{-1} and spans from 78,600 – 77,800 cm^{-1} as is depicted in Fig. 8A. Between 78,400 cm^{-1} and the atomic transition, we observe an XeAr band system assigned as the $0^+ \rightarrow \rightarrow 1$ transition dissociating to the Xe* $6p$ [5/2]$_3$ limit. [24] This band system exhibits relatively low intensity because it is associated with an atomic transition
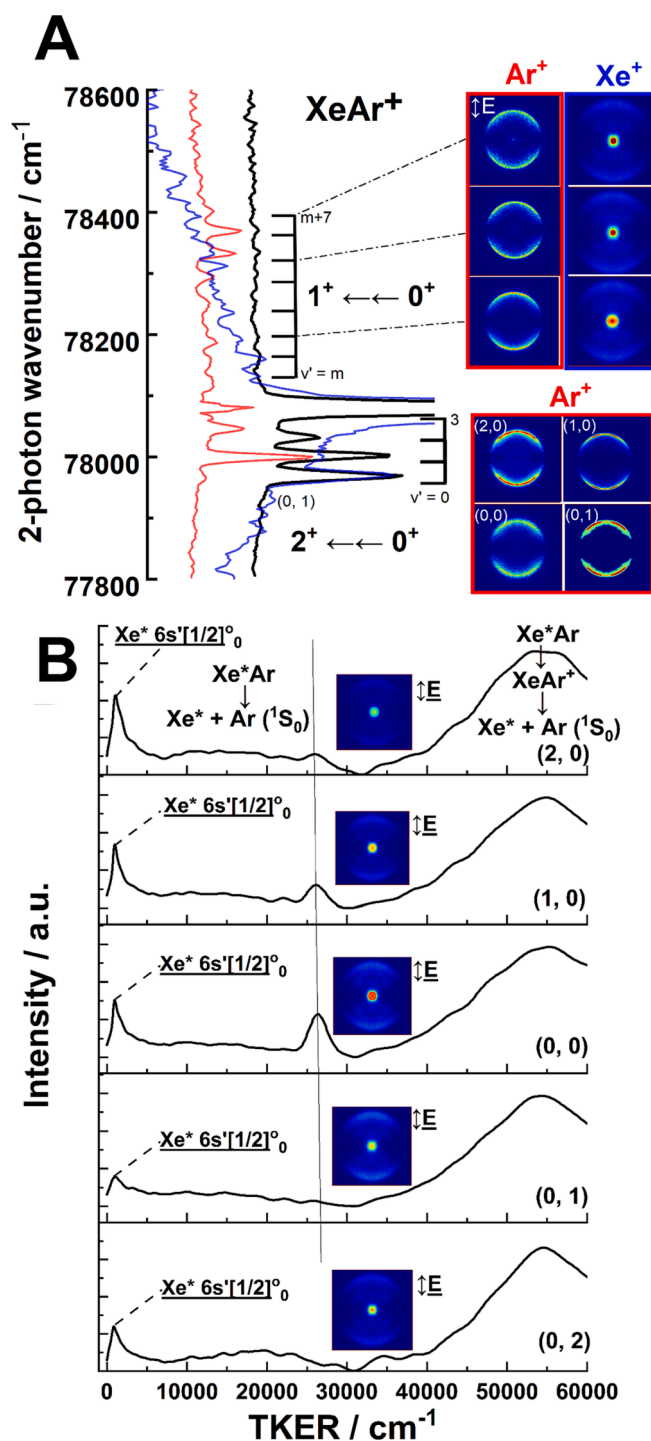

Fig. 8. (**A**) REMPI (black trace) and UVPD spectra (blue trace, Xe$^+$; red trace, Ar$^+$) in the vicinity of the Xe* $6p$ [5/2]$_2$ atomic transition. Associated photofragment images are overlaid. (**B**) TKER spectra observed via the $2 \leftarrow 0^+$ vibronic bands.

forbidden by the ΔJ selection rule. Throughout the entire spectral range, the only low TKER channel observed experimentally is the Xe* 6s' [1/2]$_1^0$ limit. All low TKER Xe$^+$ photofragments are isotropic.

Three-photon dissociation to yield Ar$^+$ produces Ar*4p'[3/2]$_2$ via the v' = (m + 6) – (m + 3) bands at approximately 78,280 cm^{-1}, and Ar*4p'[1/2]$_1$ for the rest of the band system. Khodorokovskii reports an additional weak band system observed in the two- and three-photon channels from 78,260 – 77,974 cm^{-1}, which coincides with the change that we observe in Ar$^+$ products. Khodorokovskii tentatively assigned this transition to be associated with the Xe* 6p [5/2]$_3$ separated atom limit and concluded that this transition was either the $0^+ \rightarrow \rightarrow 3$ or $0^+ \rightarrow \rightarrow 2$ transition dissociating to Xe* 6p[5/2]$_3$.[24] Angular distributions for all Ar$^+$ photofragments in this region are similar; large β_2 with small contributions from the higher order terms. As such, we can offer no further clarification as to which excited state is accessed in this region.

3.6.2. Transitions below 78,100 cm^{-1}

The lowest energy transition observed occurs as a short vibrational progression in the 77,800 – 78,100 cm^{-1} region to the red of the Xe* 6p [5/2]$_2$ atomic line. This band has been assigned as the $0^+ \rightarrow \rightarrow 2$ transition dissociating to Xe* 6p [5/2]$_2$ products.[24] As shown in Fig. 8, this transition exhibits strong signals in the Xe* 6s' [1/2]$_1^0$ channel and Ar*4p'[1/2]$_1$ product channels. Another Xe$^+$ signal is observed at TKER $\sim$ 28,000 cm^{-1}, but we are not able to definitively assign the associated product channel (see Fig. 8B). Low TKER Xe$^+$ photofragments are isotropic.

Ar$^+$ photoproducts for this band system exhibit a $\cos^2\theta$ angular distribution ($\beta_2 \approx 2$). This implies either a $0^+ \rightarrow 0^+ \rightarrow 0^+ \rightarrow 1$, $0^+ \rightarrow 0^+ \rightarrow 1 \rightarrow 1$ or $0^+ \rightarrow 1 \rightarrow 1 \rightarrow 1$ excitation. Given the band assignments of Khodorokovskii, and the fact that the $0^+ \rightarrow \rightarrow 1$ transition to higher wavenumber could extend to (but is not observed in) the region of the $0^+ \rightarrow \rightarrow 2$ transition, it is possible that mixing of the excited states gives rise to the observed Ar$^+$ angular distributions.

4. Conclusions

This work presents an in-depth analysis of the dissociation dynamics of XeAr in the 77,500 – 81,000 cm^{-1} region. Photofragment images were recorded via 38 vibronic bands associated with at least nine different electronic transitions. The complex electronic structure of XeAr in this region gives rise to both Xe$^+$ and Ar$^+$ photofragments, and highly localized perturbations (*e.g.*, Xe* 5d [1/2]$_1^0$, *ca.* 78,956 cm^{-1}) as observed in dramatically varying product branching ratios and angular distributions. A global analysis of the observed product channels enables calculation of D$_0$ = 114.4 $\pm$ 2.7 cm^{-1}, which is in accordance with the previous measurement of 117.8 cm^{-1} (See Table S2).[21] Notably, we observe two previously unreported vibronic band systems which we assign as the $0^+ \rightarrow \rightarrow 0^+$ electronic transitions, dissociating to the Xe* 5d [3/2]$_2^0$ (*ca.* 80,323 cm^{-1}) and Xe* 5d [7/2]$_3^0$ (*ca.* 80,970 cm^{-1}) limits.

By monitoring Xe* photoproducts as a function of laser frequency, we could unambiguously assign product channels to specific dissociation pathways. In performing regression on these channels, neutral products had a slope of one at the two-photon level and an intercept that corresponds to the sum of the dissociation threshold and the ground state dissociation energy of neutral XeAr. Product channel assignments highlighted several vibronic bands and local perturbations that were previously undocumented (see Table S1 for details).

Similar analysis that was conducted for the Ar* photofragments revealed dissociation at the three-photon level. Our results indicate that this must occur via ion-core switching and dissociation of a superexcited Ar*Xe state. To the best of our knowledge, this is the first observation of Ar* photofragments generated via ion core switching to access an Ar*Xe superexcited state using the VMI technique. Recoil anisotropy analysis of the photoproducts allowed us to further understand the symmetry of

the intermediate states (*i.e.,* $0^+ \rightarrow 0^+ \rightarrow 0^+ \rightarrow 1$) and their relative lifetimes.

We also successfully documented high TKER (*ca.* 60,000 cm^{-1}) Xe$^+$ channels characteristic of dissociative photoionization. These product channels likely represent a type of (2 + 2) excitation followed by dissociation from the inner turning point of an excited XeAr$^+$ curve (most likely one of the X $^2\Sigma_{1/2}$ and A_1 $^2\Pi_{3/2}$ curves). This behavior is similar to the process that what was observed for the xenon dimer.[63]

This work underscores the utility of employing action spectroscopy and velocity map imaging concurrently. Application of these techniques have enabled new insights into the complex electronic structure associated with the Ryberg states of XeAr. While theoretical calculations capture much of the excited state structure, several gaps persist in the understanding of experimentally observed product channels and how excited states couple (*e.g.,* there is no current set of known Ar*Xe curves). In that regard, theoretical studies of vibronic coupling between Xe*Ar exited states and calculation of Ar*Xe excited states is needed for a more complete understanding of XeAr photophysical processes.

CRediT authorship contribution statement

Cailum M.K. Stienstra: Writing – original draft, Software, Methodology, Investigation, Formal analysis, Data curation, Conceptualization. **Alexander Haack:** Writing – review & editing, Formal analysis. **Arthur Lee:** Investigation. **W. Scott Hopkins:** Writing – review & editing, Supervision, Investigation, Funding acquisition, Formal analysis, Conceptualization.

Declaration of competing interest

Data availability

Data will be made available on request.

Acknowledgements

Appendix A. Supplementary material

Supplementary data to this article can be found online at https://doi.org/10.1016/j.chemphys.2024.112254.

References

[1] I. Dmochowski, Xenon out of Its Shell, Nat. Chem. 1 (3) (2009) 250, https://doi.org/10.1038/nchem.230.

[2] L. Pauling, The formulas of antimonic acid and the antimonates, J. Am. Chem. Soc. 55 (5) (1933) 1895–1900, https://doi.org/10.1021/ja01332a016.

[3] C.K. Jørgensen, G. Frenking, Historical, Spectroscopic and Chemical Comparison of Noble Gases BT - Noble Gas and High Temperature Chemistry; Springer Berlin Heidelberg: Berlin, Heidelberg, 1990; pp 1–15.

[4] N. Bartlett, S.P. Beaton, N.K. Jha, Oxidizing trends in the third-transition-series hexafluorides, Chem. Commun. (london) 6 (1966) 168–169, https://doi.org/10.1039/C19660000168.

[5] S. Seidel, K. Seppelt, Xenon as a complex ligand: the tetra xenono Gold(II) cation in AuXe(4)2+(Sb(2)F(11)-)(2), Science 290 (5489) (2000) 117–118, https://doi.org/10.1126/science.290.5489.117.

[6] L. Casperson, A. Yariv, Pulse Propagation in a High-Gain Medium, Phys. Rev. Lett. 26 (6) (1971) 293–295, https://doi.org/10.1103/PhysRevLett.26.293.

[7] I.A. Kügler, Xenon lamps in film and television, J. SMPTE 77 (6) (1968) 633–636, https://doi.org/10.5594/J05811.

[8] P.B. Chu, J.T. Chen, R. Yeh, G. Lin, J.C.P. Huang, B.A. Warneke, S.J. Pister, Controlled Pulse-Etching with Xenon Difluoride. In *Proceedings of international solid state sensors and actuators conference (Transducers' 97)*; 1997; Vol. 1, pp 665–668.

[9] B.D. Jordan, E.L. Wright, Xenon as an anesthetic agent, AANA J. 78 (5) (2010) 387–392.

[10] T.S. Aziz, Xenon in anesthesia, Int. Anesthesiol. Clin. 39 (2001) 2.

[11] D.L. Bushnell, K.B. Sood, P. Shirazi, I. Pal, Evaluation of pulmonary perfusion in lung regions showing isolated xenon-133 ventilation washout defects, Clin. Nucl. Med. 15 (8) (1990) 562–565, https://doi.org/10.1097/00003072-199008000-00009.

[12] R.A. Muller, S.E. Derenzo, G. Smadja, D.B. Smith, R.G. Smits, H. Zaklad, L. W. Alvarez, Liquid-filled proportional counter, Phys. Rev. Lett. 27 (8) (1971) 532–535, https://doi.org/10.1103/PhysRevLett.27.532.

[13] P. Di Gangi, The xenon road to direct detection of dark matter at LNGS: The XENON project, Universe 7 (8) (2021), https://doi.org/10.3390/universe7080313.

[14] S. Kawai, A.S. Foster, T. Björkman, S. Nowakowska, J. Björk, F.F. Canova, L. H. Gade, T.A. Jung, M.E. Van Der, Waals interactions and the limits of isolated atom models at interfaces, Nat. Commun. 7 (1) (2016) 11559, https://doi.org/10.1038/ncomms11559.

[15] C.L. Gordon, B. Feldman, C.P. Christensen, Microwave-Discharge excitation of an ArXe laser, Opt. Lett. 13 (2) (1988) 114–116, https://doi.org/10.1364/OL.13.000114.

[16] C. Laigle, F. Collier, Kinetic Study of (ArXe+) heteronuclear Ion in electron beam excited Ar-Xe Mixture, J. Phys. B: At. Mol. Phys. 16 (4) (1983) 687–697, https://doi.org/10.1088/0022-3700/16/4/021.

[17] C. Huang, M. Zhong, Z. Wu, Anomalous ellipticity dependence in nonsequential double ionization of ArXe, Sci. Rep. 8 (1) (2018) 8772, https://doi.org/10.1038/s41598-018-27120-x.

[18] L.P. Rakcheeva, P.Y. Serdobintsev, A.A. Belyaeva, I.A. Shevkunov, A.S. Melnikov, A.A. Nakozina, A.A. Pastor, M.A. Khodorkovskii, Mass-resolved two-photon and photoelectron spectra of ArXe in the region of Xe* 7p, 6p′, 6d, J. Chem. Phys. 139 (17) (2013) 174304, https://doi.org/10.1063/1.4827476.

[19] D.M. Mao, X.K. Hu, S.S. Dimov, R.H. Lipson, Electronic symmetry assignments for the ArXe and KrXe band systems in the vicinity of the Xe* 6s′[1/2]O1 ← Xe(1S0) resonance Line, J. Phys. B Atomic Mol. Phys. 29 (3) (1996) L89–L94, https://doi.org/10.1088/0953-4075/29/3/002.

[20] S.S. Dimov, X.K. Hu, D.M. Mao, J.Y. Cai, R.H. Lipson, Mass resolved two-photon spectra of ArXe in the region of Xe*(6p), J. Chem. Phys. 104 (1996) 1213–1224.

[21] C.D. Pibel, K. Ohde, K. Yamanouchi, Tunable vacuum ultraviolet laser spectroscopy of XeAr and XeNe near 68 000 Cm−1: Interatomic potentials mediated by a 6s Rydberg electron, J. Chem. Phys. 105 (5) (1996) 1825–1832, https://doi.org/10.1063/1.472081.

[22] M.A. Khodorkovskiĭ, A.A. Belyaeva, L.P. Rakcheeva, P.Y. Serdobintsev, A.A. Pastor, A.S. Mel'nikov, N.A. Timofeev, R. Hallin, K. Seigbahn, Study of the lowest electronic states of Xe2, XeKr, and XeAr molecules by the method of multiphoton resonance ionization, Opt. Spectrosc. 104 (5) (2008) 674, https://doi.org/10.1134/S0030400X08050068.

[23] M.A. Khodorkovskii, S.V. Murashov, T.O. Artamonova, A.A. Beliaeva, L.P. Rakcheeva, A.A. Pastor, P.Y. Serdobintsev, N.A. Timofeev, I.A. Shevkunov, I.A. Dement'ev, J. Nordgren, Electronic Spectra of ArXe Molecules in the Region of Xe* (5d, 7s, 7p, 6p′), 80 300–89 500 Cm−1, Using Resonantly Enhanced Multiphoton Ionization, *J. Phys. B: Atomic, Mol. Opt. Phys. 43* (23) (2010) 235101. https://doi.org/10.1088/0953-4075/43/23/235101.

[24] M.A. Khodorkovskii, S.V; Murashov, T.O. Artamonova, A.A. Beliaeva, L.P. Rakcheeva, A.A. Pastor, P.Y. Serdobintsev, N.A. Timofeev, I.A. Shevkunov, I.A. Dement'ev, J. Nordgren, Electronic Spectra of ArXe Molecules in the Region of Xe* (6s′, 6p, 5d), 77 000–80 200 Cm^{-1}, Using Resonantly Enhanced Multiphoton Ionization, *J. Phys. B: Atomic, Mol. Optical Phys. 43* (15) (2010) 155101. https://doi.org/10.1088/0953-4075/43/15/155101.

[25] T. Tsuchizawa, K. Yamanouchi, S. Tsuchiya, Interatomic Potentials of the C1 and D0+ States of XeNe, XeAr, and XeKr as studied by tunable vacuum ultraviolet laser spectroscopy, J. Chem. Phys. 92 (3) (1990) 1560–1567, https://doi.org/10.1063/1.458087.

[26] O. Zehnder, F. Merkt, The low-lying electronic states of ArXe+ and their potential energy functions, J. Chem. Phys. 128 (1) (2008) 14306, https://doi.org/10.1063/1.2815801.

[27] L. Piticco, F. Merkt, Rotationally resolved PFI-ZEKE photoelectron Spectroscopic study of the low-lying electronic states of ArXe+, J. Chem. Phys. 137 (9) (2012) 94308, https://doi.org/10.1063/1.4747549.

[28] L. Piticco, M. Schäfer, F. Merkt, Structure and dynamics of the electronically excited C 1 and D 0+ states of ArXe from high-resolution vacuum ultraviolet

[29] spectra, J. Chem. Phys. 136 (7) (2012) 74304, https://doi.org/10.1063/1.3682770.

[29] L. Piticco, F. Merkt, A.A. Cholewinski, F.R.W. McCourt, R.J. Le Roy, Rovibrational structure and potential energy function of the X0+ ground electronic state of ArXe, J. Mol. Spectrosc. 264 (2) (2010) 83–93. https://doi.org/10.1016/j.jms.2010.08.007.

[30] O. Zehnder, High-Resolution Spectroscopic Investigations of Rare Gas Atoms and Dimers, ETH Zurich, 2008.

[31] S.T. Pratt, P.M. Dehmer, J.L. Dehmer, Electronic spectra of NeXe, ArXe, and KrXe using resonantly enhanced multiphoton ionization, J. Chem. Phys. 83 (11) (1985) 5380–5390, https://doi.org/10.1063/1.449707.

[32] P.M. Dehmer, S.T. Pratt, Photoionization of ArKr, ArXe, and KrXe and bond dissociation energies of the rare gas dimer ions, J. Chem. Phys. 77 (1982) 4804, https://doi.org/10.1063/1.443721.

[33] H. Yoshii, T. Tanaka, Y. Morioka, T. Hayaishi, K. Ito, Vibrationally resolved threshold photoelectron-photoion coincidence spectra of KrXe, J. Chem. Phys. 111 (23) (1999) 10595–10601, https://doi.org/10.1063/1.480412.

[34] K.P. Huber, R.H. Lipson, The emission spectrum of ArXe+ from a supersonic jet discharge, J. Mol. Spectrosc. 119 (2) (1986) 433–445. https://doi.org/10.1016/0022-2852(86)90038-X.

[35] A. Goldberg, J. Jortner, Structural relaxation dynamics of electronically excited XeArN clusters, J. Chem. Phys. 107 (21) (1997) 8994–9017, https://doi.org/10.1063/1.475191.

[36] G. Nowak, J. Fricke, The heteronuclear excimers ArKr*, ArXe*, KrXe*, J. Phys. B: At. Mol. Phys. 18 (7) (1985) 1355–1367, https://doi.org/10.1088/0022-3700/18/7/016.

[37] M.V. Bobetic, J.A. Barker, Vibrational levels of heteronuclear rare gas van Der Waals molecules, J. Chem. Phys. 64 (6) (1976) 2367–2369, https://doi.org/10.1063/1.432524.

[38] R.H. Lipson, R.W. Field, Toward a global and causal understanding of the unusual Rydberg state potential energy curves of the heteronuclear rare gas dimers, J. Chem. Phys. 110 (22) (1999) 10653–10656, https://doi.org/10.1063/1.479009.

[39] A.P. Hickman, D.L. Huestis, R.P. Saxon, Interatomic potentials for excited states of XeHe and XeAr, J. Chem. Phys. 96 (3) (1992) 2099, https://doi.org/10.1063/1.462061.

[40] Mr. C MK Stienstra, Dr. N. Coughlan, Dr. A. Haack, Dr. P.J. Carr, Dr. J. Crouse, Dr. J. Featherstone, Prof. S. Hopkins, Investigating the Rydberg States and Photodissociation Dynamics of Kr₂ Using Velocity Map Imaging. 2023. https://doi.org/10.1139/CJC-2022-0283.

[41] *NIST Chemistry WebBook, SRD 69*. National Institute of Standards and Technology.

[42] A.J.R. Heck, D.W. Neyer, R.N. Zare, D.W. Chandler, Photofragment Imaging of Kr2 and ArKr van Der Waals molecules following two-photon excitation, J. Phys. Chem. 99 (50) (1995) 17700–17710, https://doi.org/10.1021/j100050a006.

[43] Y. Fukuda, T. Szidarovszky, M. Nakata, A. Hishikawa, K. Yamanouchi, Ion-Core Switching in Rydberg Series of XeKr. 2023.

[44] C. Vallance, Molecular Photography: Velocitymap Imaging of Chemical Events, *Philosophical Transactions of the Royal Society of London. Series A: Mathematical, Physical and Engineering Sciences* 2004, *362* (1825), 2591–2609. https://doi.org/10.1098/RSTA.2004.1460.

[45] R.N. Zare, Photoejection Dynamics (1972).

[46] R.K. Sander, K.R. Wilson, Double absorption photofragment spectroscopy: a new tool for probing unimolecular processes, J. Chem. Phys. 63 (10) (1975) 4242–4251, https://doi.org/10.1063/1.431195.

[47] R.N. Dixon, Recoil anisotropy following multiphoton dissociation via near-resonant intermediate states, J. Chem. Phys. 122 (19) (2005) 194302, https://doi.org/10.1063/1.1896951.

[48] M.N.R. Ashfold, N.H. Nahler, A.J. Orr-Ewing, O.P.J. Vieuxmaire, R.L. Toomes, T. N. Kitsopoulos, I.A. Garcia, D.A. Chestakov, S.-M. Wu, D.H. Parker, Imaging the dynamics of gas phase reactions, PCCP 8 (1) (2006) 26–53, https://doi.org/10.1039/B509304J.

[49] G.M. Roberts, J.L. Nixon, J. Lecointre, E. Wrede, J.R.R. Verlet, Toward real-time charged-particle image reconstruction using polar onion-peeling, Rev. Sci. Instrum. 80 (5) (2009) 53104, https://doi.org/10.1063/1.3126527.

[50] S. Gibson, D.D. Hickstein, R. Yurchak, M. Ryazanov, D. Das, G. Shih, PyAbel/PyAbel: V0.8.4. 2021. https://doi.org/10.5281/ZENODO.4690660.

[51] G. Herzberg, *Spectra of Diatomic Molecules*; Van Norstrand: Princeton, 1950.

[52] A. Wolf, M. Reiher, B.A. Hess, The generalized douglas-kroll transformation, J. Chem. Phys. 117 (20) (2002) 9215–9226, https://doi.org/10.1063/1.1515314.

[53] T. Noro, M. Sekiya, T. Koga, Segmented contracted basis sets for atoms H through Xe: sapporo-(DK)-NZP sets (n = D, T, Q), Theor. Chem. Acc. 131 (2) (2012) 1–8, https://doi.org/10.1007/S00214-012-1124-Z.

[54] T. Noro, M. Sekiya, T. Koga, Sapporo-(DKH3)-NZP (n 5 D, T, Q) sets for the sixth period s-, d-, and p-block atoms, Theor. Chem. Acc. 132 (5) (2013) 1–5, https://doi.org/10.1007/S00214-013-1363-7.

[55] I. Mayer, Bond order and valence indices: a personal account, J. Comput. Chem. 28 (1) (2007) 204–221, https://doi.org/10.1002/JCC.20494.

[56] F. Neese, F. Wennmohs, U. Becker, C. Riplinger, The ORCA quantum chemistry program package, J. Chem. Phys. 152 (22) (2020), https://doi.org/10.1063/5.0004608/1061982.

[57] F. Neese, J. Wiley, The ORCA program system, Wiley Interdiscip. Rev.: Comput. Mol. Sci. 2 (1) (2012) 73–78, https://doi.org/10.1002/WCMS.81.

[58] R.S.F. Chang, H. Horiguchi, D.W. Setser, Radiative lifetimes and two-body collisional deactivation rate constants in argon for Kr(4p 55p) and Kr(4p 55p′) States, J. Chem. Phys. 73 (2) (2008) 778, https://doi.org/10.1063/1.440185.

[59] A.M. Bush, J.M. Dyke, P. Mack, D.M. Smith, T.G. Wright, Production of Rg+ ions in the resonance-enhanced multiphoton ionization spectroscopy of Rg · NO (Rg = Ar,

Kr and Xe), Chem. Phys. 223 (2–3) (1997) 239–249, https://doi.org/10.1016/ S0301-0104(97)00238-3.

[60] W.S. Hopkins, M.L. Lipciuc, S.H. Gardiner, C. Vallance, RG+ formation following photolysis of NO-RG via the Ã-X̃ transition: a velocity map imaging study, J. Chem. Phys. 135 (3) (2011) 34308, https://doi.org/10.1063/1.3610415/190171.

[61] C.E. Moore, NIST Atomic Energy Levels: As Derived from the Analyses of Optical Spectra; Volume II, First.; Washington D.C., 1972.

[62] X.K. Hu, D.M. Mao, S.S. Dimov, R.H. Lipson, Mass-resolved two-photon spectra of Xe2 in the region of Xe*(5d). I. Vibronic Analyses, *J. Chem. Phys.* 106 (23) (1998) 9411, https://doi.org/10.1063/1.473846.

[63] W.S. Hopkins, S.R. Mackenzie, Dissociation dynamics of the low-lying Rydberg states of Xe2: a velocity map imaging study, Mol. Phys. 110 (19–20) (2012) 2465–2475, https://doi.org/10.1080/00268976.2012.698027.

[64] T. Sato, T. Kinugawa, T. Arikawa, M. Kawasaki, Two-photon dissociation of SO2 in the ultraviolet region, Chem. Phys. 165 (1) (1992) 173–182, https://doi.org/ 10.1016/0301-0104(92)80054-Y.